





## Magnetic properties of the quasicrystal approximant $\text{Au}_{65}\text{Ga}_{21}\text{Tb}_{14}$

Kazuhiro Nawa <sup>1</sup>, Maxim Avdeev <sup>2,3</sup>, Asuka Ishikawa,<sup>4</sup> Hiroyuki Takakura,<sup>5</sup> Chin-Wei Wang <sup>6,2</sup>, Daisuke Okuyama,<sup>1</sup> Ryo Murasaki,<sup>1</sup> Ryuji Tamura <sup>7</sup> and Taku J. Sato<sup>1</sup>

<sup>1</sup>*Institute of Multidisciplinary Research for Advanced Materials, Tohoku University, 2-1-1 Katahira, Aoba, Sendai 980-8577, Japan*

<sup>2</sup>*Australian Centre for Neutron Scattering, Australian Nuclear Science and Technology Organisation, New Illawarra Road, Lucas Heights, New South Wales 2234, Australia*

<sup>3</sup>*School of Chemistry, The University of Sydney, Sydney, New South Wales 2006, Australia*

<sup>4</sup>*Research Institute for Science and Technology, Tokyo University of Science, Tokyo 125-8585, Japan*

<sup>5</sup>*Faculty of Engineering, Hokkaido University, Sapporo, Hokkaido 060-8628, Japan*

<sup>6</sup>*National Synchrotron Radiation Research Center, Hsinchu 30076, Taiwan*

<sup>7</sup>*Department of Materials Science and Technology, Tokyo University of Science, Tokyo 125-8585, Japan*



(Received 14 March 2022; revised 4 April 2023; accepted 9 May 2023; published 31 May 2023)

The magnetic properties of the quasicrystal approximant  $\text{Au}_{65}\text{Ga}_{21}\text{Tb}_{14}$  were investigated using magnetization and neutron diffraction experiments. The temperature dependences of the magnetic susceptibility and magnetization curve indicate dominant ferromagnetic interactions, whereas a whirling antiferromagnetic order was observed in neutron diffraction experiments. In the antiferromagnetic phase, the magnetic moments are aligned almost perpendicular to a pseudofivefold symmetry axis, which corresponds to the easy-axis direction of a Tb atom. Magnetic properties similar to those of  $\text{Au}_{72}\text{Al}_{14}\text{Tb}_{14}$  in spite of the substantial difference in the Au concentration suggest the robustness of the easy-axis anisotropy against the chemical environment.

DOI: [10.1103/PhysRevMaterials.7.054412](https://doi.org/10.1103/PhysRevMaterials.7.054412)

### I. INTRODUCTION

Magnetism in quasicrystals and quasicrystal approximants has attracted interest owing to the expectation of nontrivial ground states. Studies on magnetic quasicrystal and quasicrystal approximants have accelerated since stable binary quasicrystals and quasicrystal approximants were discovered [1,2]. The occurrence of long-range antiferromagnetic order was observed in the 1/1 quasicrystal approximant  $\text{Cd}_6R$  ( $R$ : rare-earth elements) [3] and confirmed by resonant x-ray scattering [4] and neutron diffraction experiments [5]. However, a reliable magnetic structure has not yet been obtained owing to the presence of a structural phase transition: the orientational ordering of a  $\text{Cd}_4$  tetrahedron located at the center of each Tsai-type cluster lowers the crystal symmetry and induces several structural domains [6,7]. Therefore, it is desirable to investigate quasicrystal approximants without a structural phase transition to understand their magnetic properties better.

Recent neutron diffraction experiments have revealed that some magnetic quasicrystal approximants [8–11] exhibit noncollinear magnetic structures [12–15]. These quasicrystal approximants belong to the space group of  $Im\bar{3}$ , as do other 1/1 quasicrystal approximants, and do not exhibit structural phase transitions at low temperatures. Magnetic  $\text{Tb}^{3+}$  ions form nearly icosahedral clusters. In the 1/1 quasicrystal approximant  $\text{Au}_{72}\text{Al}_{14}\text{Tb}_{14}$ , magnetic moments are aligned almost tangentially to the cluster surface. They follow a threefold symmetry around the [111] axis, leading to a whirling arrangement. The neighboring magnetic clusters are coupled antiferromagnetically [12]. The whirling antiferromagnetic order was also observed in a single crystalline diffraction study of  $\text{Au}_{70}\text{Al}_{16}\text{Tb}_{14}$  [15]. In addition, the 1/1

quasicrystal approximant  $\text{Au}_{70}\text{Si}_{17}\text{Tb}_{13}$  exhibits a magnetic structure associated with that of  $\text{Au}_{72}\text{Al}_{14}\text{Tb}_{14}$ . The former magnetic structure can be roughly derived by reversing half of the magnetic moment of the latter magnetic structure. Consequently, large spontaneous magnetic moments appear along the [111] direction [13].

Previous studies have indicated that competing magnetic interactions and the formation of magnetic clusters are key components in stabilizing noncollinear magnetic structures. Accordingly, in principle, various noncollinear magnetic structures could be realized by tuning the magnetic interactions or magnetic anisotropy of  $\text{Tb}^{3+}$  ions [16,17]. As magnetic interactions are dominated by the Ruderman-Kittel-Kasuya-Yosida (RKKY) mechanism, magnetic interactions within an icosahedral cluster can be adjusted by tuning the electrons-per-atom ratio  $e/a$  [8,9,18]. In addition, changing the local environment around  $\text{Tb}^{3+}$  ions could result in a change in the easy anisotropy axis [16,19]. The magnetic properties of quasicrystal approximants with different compositions should reflect the changes in the  $e/a$  and easy anisotropy axes. The magnetic structures of quasicrystal approximants need to be revealed to understand the general trend in magnetic quasicrystal approximants and quasicrystals.

In this paper, we report the magnetic properties and magnetic structure of the Au-Ga-Tb 1/1 quasicrystal approximant [20]. We focus on the magnetic properties of  $\text{Au}_{65}\text{Ga}_{21}\text{Tb}_{14}$ , which belongs to the space group of  $Im\bar{3}$  (Table I). Its  $e/a$  of 1.70 is located near the boundary of the antiferromagnetic and ferromagnetic phases and is much larger than the value of 1.56 for  $\text{Au}_{72}\text{Al}_{14}\text{Tb}_{14}$ , which is located near the other boundary of the antiferromagnetic phase [18]. In addition, its composition is very close to that of a magnetic quasicrystal that exhibits

TABLE I. Crystallographic data and refinement parameters of the single-crystal x-ray structure analysis.

Crystallographic data and refinement parameters	
Space group	$Im\bar{3}$
$a$ (Å)	14.72530(10)
$V$ (Å <sup>3</sup> )	3192.95(7)
Calculated density (g/cm <sup>3</sup> )	8.577
Temperature (K)	293
$h$ range	$-20 \leq h \leq 19$
$k$ range	$-20 \leq k \leq 20$
$l$ range	$-20 \leq l \leq 19$
$F(000)$	6696
Reflections collected	48 241
Independent reflections	897
Data <sup>a</sup> /restraints/parameters	869/0/70
$R$ indices for observed reflections ( $R$ , $R_w$ ) <sup>b</sup>	0.0208, 0.0370
Goodness of fit on $F$	1.336

<sup>a</sup>Reflections with  $I > 2\sigma$  are used for the refinement.

<sup>b</sup> $R = \sum (|F_{\text{obs}}|^2 - |F_{\text{calc}}|^2) / \sum |F_{\text{obs}}|^2$ ,  $wR = \sum w(|F_{\text{obs}}|^2 - |F_{\text{calc}}|^2) / \sum w|F_{\text{obs}}|^2$ ,  $w = 1 / \{\sigma^2(|F_{\text{obs}}|^2) + 247.1726(|F_{\text{obs}}|^2 + 2|F_{\text{calc}}|^2)/3\}$ .

long-range magnetic order [21]. Powder neutron diffraction experiments revealed a whirling antiferromagnetic arrangement of the magnetic moments in Au<sub>65</sub>Ga<sub>21</sub>Tb<sub>14</sub>, which is similar to that observed for Au<sub>72</sub>Al<sub>14</sub>Tb<sub>14</sub> [12]. The whirling antiferromagnetic order realized over a wide range of  $e/a$  values indicates the robustness of the quasicrystal approximant against chemical substitution.

## II. EXPERIMENTS

Polycrystalline samples of Au<sub>65</sub>Ga<sub>21</sub>Tb<sub>14</sub> were synthesized by arc melting using high-purity Au, Ga, and Tb as the starting materials. The alloy was then annealed at 1073 K for 50 h under Ar atmosphere, followed by quenching in chilled water. The sample quality was confirmed using powder x-ray diffraction (XRD) experiments with Cu  $K\alpha$  radiation (Rigaku MiniFlex 600 and Rigaku Ultima IV). The magnetic properties were investigated using a superconducting quantum interference device magnetometer (Quantum Design magnetic property measurement system).

Crystal structure analysis was performed for a single crystal selected from a polycrystalline sample with an XtaLAB Synergy-R single-crystal diffractometer equipped with a hybrid pixel array detector (HyPix-6000, Rigaku) using Mo  $K\alpha$  radiation ( $\lambda = 0.71073$  Å). The indexing and integration of the diffraction intensities were performed using the CRYSTALIS PRO software [22]. The initial structural model was obtained using a dual-space method using SHELXT [23]. Subsequent structural refinements were performed using SHELXL [24].

Neutron powder diffraction experiments were performed using the high-resolution powder diffractometer ECHIDNA installed in the Open Pool Australian Lightwater (OPAL) reactor, Australian Nuclear Science and Technology Organisation, to investigate the magnetic structure [25]. Neutrons with  $\lambda = 2.4395$  Å were selected using the Ge 331 reflections. A polycrystalline sample (2 g) was loaded in a vanadium can with a diameter of 6 mm. The bottom part of the vanadium can

was filled with a Cd absorber to adjust the sample position. The sample can was set on the cold head of a closed cycle <sup>4</sup>He refrigerator with a base temperature of 4 K. The intensities were collected at base temperatures of 4 and 20 K. In addition, the temperature dependence of the magnetic reflection was investigated using the general purpose triple-axis spectrometer 4G GPTAS installed in the Japan Research Reactor 3 (JRR-3), Tokai, Japan. The spectrometer was operated in the double-axis mode without using an analyzer. The wavelength was set to  $\lambda = 2.365$  Å by using pyrolytic graphite (002) reflections. Horizontal collimations of 40'–40'–40' were employed. The powder sample (2 g) was sealed in an Al sample can with He exchange gas and cooled to 2.5 K using a closed cycle <sup>4</sup>He refrigerator.

## III. EXPERIMENTAL RESULTS

The single-crystal XRD experiments revealed some differences in the crystal structure of Au<sub>65</sub>Ga<sub>21</sub>Tb<sub>14</sub> compared with that of Au<sub>72</sub>Al<sub>14</sub>Tb<sub>14</sub>. Successive clusters formed by Au, Ga, and Tb atoms are shown in Fig. 1(a). Crystallographic data and refinement parameters are listed in Table I, and the structural parameters are summarized in Table II. First, the occupancy of the Ga atom is substantially larger at the Ga2 site, which is one of the nearest-neighbor nonmagnetic sites of the Tb atom. The atomic positions of the Ga2 sites are shown in Fig. 1(b): The occupancy was observed to be 0.513(7) in Au<sub>65</sub>Ga<sub>21</sub>Tb<sub>14</sub>, whereas it decreased to 0.098(4) for the corresponding Al2 sites (including 2A and 2B) in Au<sub>72</sub>Al<sub>14</sub>Tb<sub>14</sub> [9]. Second, the lattice constant of 14.7361 Å for Au<sub>65</sub>Ga<sub>21</sub>Tb<sub>14</sub> (estimated from the powder XRD experiments; see the Supplemental Material [27]) was slightly smaller than the value of 14.7753 Å for Au<sub>72</sub>Al<sub>14</sub>Tb<sub>14</sub> [9]. The decrease in the lattice constant can be attributed to the decrease in the occupancy of Au atoms, as the atomic size of Au is larger than that of Ga and Al. On the other hand, the distances of Tb-Tb atoms within the cluster were estimated to be 5.5043(12) and 5.5467(7) Å. These values are slightly larger than those of 5.4693 and 5.5297 Å in Au<sub>72</sub>Al<sub>14</sub>Tb<sub>14</sub>. The cluster radius, which is defined by the distance of the Tb atoms from the cluster center, is 5.2671(6) Å for Au<sub>65</sub>Ga<sub>21</sub>Tb<sub>14</sub>, whereas it is 5.2475 Å for Au<sub>72</sub>Al<sub>14</sub>Tb<sub>14</sub>. The nearly icosahedral cluster may be expanded by the Au atoms occupying the Au7A and Ga7B sites, which are near the centers of successive clusters.

The temperature dependences of the magnetic susceptibility and magnetization curve indicate the occurrence of an antiferromagnetic order despite the dominant ferromagnetic interactions. At high temperatures, the magnetic susceptibility [Fig. 2(a)] increases with decreasing temperature following the Curie-Weiss rule. The Curie-Weiss fit between 50 and 300 K yields an effective magnetic moment and Weiss temperature of 10.1(1) $\mu_B$  and 10.79(2) K, respectively. For quasicrystals and quasicrystal approximants, the magnetic susceptibility is not influenced by the anisotropy of rare-earth atoms. Generally, the local parallel and perpendicular magnetic susceptibilities of each rare-earth atom show different temperature dependences. However, these contributions are averaged over several rare-earth atoms, where the magnetic field direction becomes effectively different owing to the

TABLE II. Structure parameters of  $\text{Au}_{65}\text{Ga}_{21}\text{Tb}_{14}$  determined from the single-crystal x-ray structure analysis. The atomic coordinates are represented by fractional coordinates. The isotropic displacement parameters were adopted for atoms with small occupancies (indicated by asterisks). The equivalent isotropic (isotropic) displacement parameters  $U_{\text{eq}}$  ( $U_{\text{iso}}$ ) are listed in units of  $\text{\AA}^2$ .

Atom	Site	$x$	$y$	$z$	Occupancy	$100U_{\text{eq}}$ ( $100U_{\text{iso}}^*$ )		
Au1A	48h	0.1115(7)	0.3401(4)	0.2020(4)	0.36(5)	0.70(7)*		
Au1B	48h	0.1014(5)	0.3430(2)	0.1977(4)	0.64(5)	0.87(4)		
Ga2	24g	0	0.2345(9)	0.0900(9)	0.513(7)	4.5(6)		
Au2	24g	0	0.2392(2)	0.0812(3)	0.487(7)	1.06(4)		
Au3	24g	0	0.40396(3)	0.35250(3)	1	0.804(11)		
Au4	16f	0.14974(2)	0.14974(2)	0.14974(2)	0.980(4)	1.52(2)		
Ga5	12e	0.19441(13)	0	0.5	1	0.89(3)		
Au6A	12d	0.4061(3)	0	0	0.43(6)	0.71(18)		
Au6B	24g	0	0.4039(3)	0.0171(8)	0.27(3)	0.89(17)*		
Tb1	24g	0	0.18690(4)	0.30498(4)	1	0.655(12)		
Ga8	8c	0.25	0.25	0.25	1	1.91(5)		
Au7A	24g	0	0.0674(5)	0.0806(6)	0.162(6)	5.0(2)*		
Ga7B	24g	0	0.0891(14)	0.0464(17)	0.087(14)	1.4(7)*		
Tb2	2a	0	0	0	0.026(14)	3.0(4)*		
Atom	Site	$100U_{11}$	$100U_{22}$	$100U_{33}$	$100U_{12}$	$100U_{23}$	$100U_{31}$	$100U_{\text{eq}}$
Au1B	48h	0.67(8)	0.76(5)	1.17(5)	0.14(3)	0.12(5)	0.12(5)	0.87(4)
Ga2	24g	4.1(7)	6.1(8)	3.2(6)	1.3(4)	0	0	4.5(6)
Au2	24g	0.51(8)	1.42(8)	1.25(9)	-0.19(6)	0	0	1.06(4)
Au3	24g	0.81(2)	0.70(2)	0.90(2)	0.123(15)	0	0	0.804(11)
Au4	16f	1.52(2)	1.52(2)	1.52(2)	0.049(13)	0.049(13)	0.049(13)	1.52(2)
Ga5	12e	1.03(8)	0.60(8)	1.05(8)	0	0	0	0.89(3)
Au6A	12d	0.80(18)	0.8(6)	0.54(17)	0	0	0	0.71(18)
Tb1	24g	0.68(2)	0.47(2)	0.82(2)	0.075(18)	0	0	0.655(12)
Ga8	8c	1.91(5)	1.91(5)	1.91(5)	-0.01(6)	-0.01(6)	-0.01(6)	1.91(5)

different orientations of the principal axes. Consequently, the effect of the local anisotropy is largely suppressed in the bulk magnetic susceptibility. The bulk magnetic susceptibility at high temperatures follows the Curie-Weiss rule, with an effective moment close to the free-ion value and the Weiss temperature induced by magnetic interactions. The details are discussed in Appendixes A and B. At low temperatures, the magnetic susceptibility exhibited a sharp decrease below 13.2 K, suggesting the occurrence of an antiferromagnetic order [Fig. 2(b)]. A probable origin of the deviation between the zero-field and field-cooling curves is a spontaneous magnetization from magnetic moments with magnetic anisotropy: the magnitudes of the spontaneous moment are estimated as  $0.063\mu_{\text{B}}$  and  $0.033\mu_{\text{B}}$  from the magnetization curves at 2 and 10 K, respectively [inset of Fig. 2(d)]. At 2 K, the magnetization curve exhibits a sharp jump at 0.78 T, indicating spin-reorientation transition. A small-field hysteresis suggests that the spin-reorientation transition is a first-order one.

These magnetic properties are similar to those observed for  $\text{Au}_{72}\text{Al}_{14}\text{Tb}_{14}$  [8,9]. The transition temperature of 13.2 K is comparable to the value of 11.8 K for  $\text{Au}_{72}\text{Al}_{14}\text{Tb}_{14}$  [8]. However, the Weiss temperature of 10.79 K is a few times higher than the value of 4.2 K for  $\text{Au}_{72}\text{Al}_{14}\text{Tb}_{14}$ , indicating an enhancement of the ferromagnetic interaction. Simultaneously, the transition field of 0.78 T was almost half of the value of 1.36 T for  $\text{Au}_{72}\text{Al}_{14}\text{Tb}_{14}$  [8]. This indicates that the value of  $e/a$  is close to the phase boundary of the ferromagnetic ground state.

The occurrence of the antiferromagnetic order is observed through a comparison of the neutron diffraction patterns at 4 and 20 K, as shown in Fig. 3. Structural refinement by the Rietveld method using the data at 20 K showed good agreement, yielding structural parameters consistent with those estimated from the single-crystal XRD analysis. At 4 K, magnetic reflections were observed between nuclear reflections. The magnetic reflections can be indexed to the reflection condition  $h + k + l = \text{odd}$ , where  $h$ ,  $k$ , and  $l$  are the Miller indices. The occurrence of the antiferromagnetic order breaks the bcc symmetry. The temperature dependence of the 210 magnetic reflection intensity is shown in Fig. 2(c). The intensity began to increase below 13.2 K, where the magnetic susceptibility showed a sharp drop. The intensity observed in the range of 12.4 to 16.0 K was fitted to a power-law function proportional to  $(T_{\text{N}} - T)^{2\beta}$  with a constant background. A Gaussian function centered at  $T_{\text{N}}$  was also included to fit the diffuse scattering empirically. The fit yielded a transition temperature of  $T_{\text{N}} = 13.58(4)$  K, which is close to the value of 13.2 K estimated from the magnetic susceptibility. The critical exponent  $\beta$  is estimated as 0.56(4). This value is larger than that expected for a 3D order [28] and is close to the mean field value of 0.5. The mean field value of  $\beta$  was also observed in a single crystalline neutron diffraction study [15] and magnetization measurements of the ferromagnetic quasicrystal approximant [29]. This may suggest that long-range interactions, such as the RKKY interactions, are active and dominate critical phenomena in this compound.

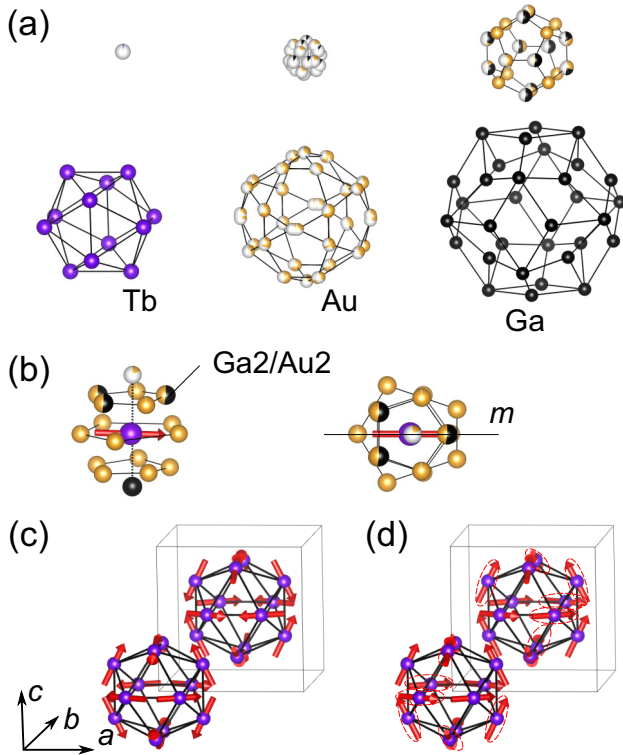


FIG. 1. (a) Successive shells of a Tsai-type cluster in  $\text{Au}_{65}\text{Ga}_{21}\text{Tb}_{14}$  obtained from single-crystal x-ray diffraction. (b) Local environment around a Tb atom. The dashed and solid lines passing through the Tb atom represent the pseudofivefold rotation axis and mirror plane, respectively. The red arrow indicates the direction of the magnetic moment in the ordered phase. Some inequivalent sites induced by disorder are merged into a single site for clarity. (c) Antiferromagnetic order in  $\text{Au}_{65}\text{Ga}_{21}\text{Tb}_{14}$ . The whirling arrangement is formed around the [111] direction. (d) Magnetic structure expected under a magnetic field. Half of the magnetic moments denoted by dashed circles are oriented in directions opposite to those illustrated in (c). The figures were obtained by using VESTA software [26].

The peak positions and intensities of the magnetic reflections are similar to those observed for  $\text{Au}_{72}\text{Al}_{14}\text{Tb}_{14}$ , suggesting the formation of a whirling antiferromagnetic order similar to that in  $\text{Au}_{72}\text{Al}_{14}\text{Tb}_{14}$ . We analyzed the magnetic structure through Rietveld refinement to confirm this hypothesis. The candidates for the initial magnetic structures were obtained using magnetic representation theory [30]. The magnetic representations for the Tb moments were decomposed using the irreducible representations (IRs) of the  $k$  group with  $k = (1, 1, 1)$ . The results of the decomposition and the corresponding magnetic basis vectors for all the IRs were obtained [31]. Good agreement was achieved by the fit based on IR2, as shown by the black solid curves in Fig. 3(a). Figure 1(c) shows the magnetic order obtained from refinement. The magnetic moments follow a threefold rotation symmetry around the [111] direction, forming a whirling magnetic order similar to that observed in  $\text{Au}_{72}\text{Al}_{14}\text{Tb}_{14}$  [12]. Each magnetic moment must remain in the local mirror plane by symmetry. In addition, it is aligned almost perpendicular to the pseudofivefold symmetry axis, as shown in Fig. 1(b). The whirling magnetic

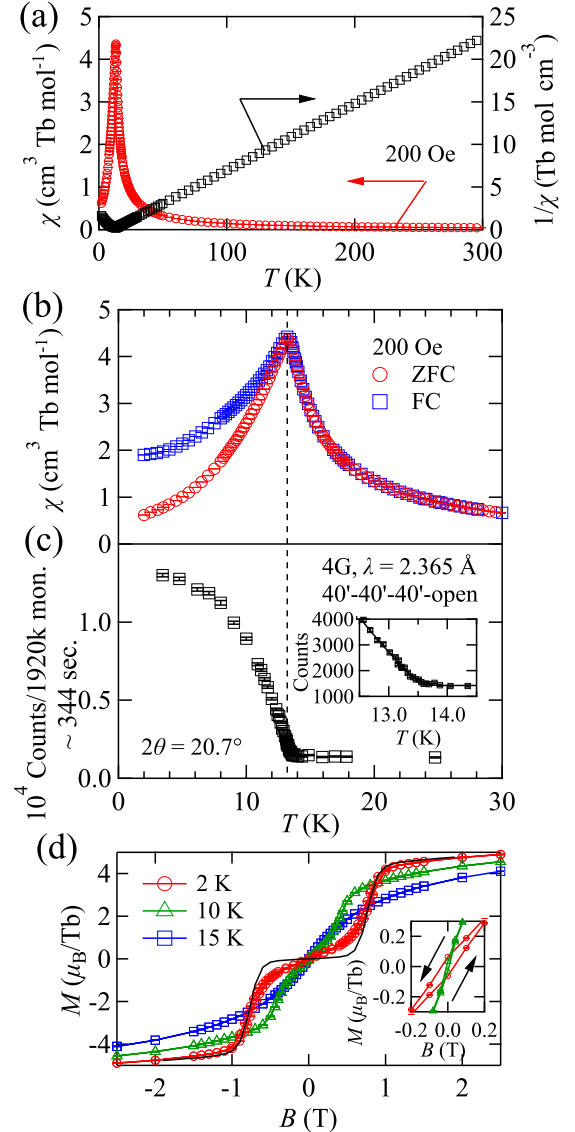


FIG. 2. (a) Temperature dependence of the magnetic susceptibility and inverse susceptibility. (b) Magnetic susceptibility below 30 K measured using zero-field-cooling and field-cooling protocols. (c) Temperature dependence of the 210 magnetic reflection intensity at  $20.7^\circ$ . The inset shows the temperature dependence near  $T_N$ . The dashed curve represents a fit to the power-law function (see the text for details). (d) Magnetization curves at 2, 10, and 15 K. The black solid curve represents the simulated curve of a single cluster with the ferromagnetic interactions  $J_1 = 0.02$  K and  $J_2 = 0.13$  K. The inset shows the enlarged view at a near-zero field.

order is represented by the two coefficients of basis vectors. They were estimated to be  $7.04(12)\mu_B$  and  $-3.49(17)\mu_B$  in  $\text{Au}_{65}\text{Ga}_{21}\text{Tb}_{14}$ . The moment direction was almost the same as that of  $\text{Au}_{72}\text{Al}_{14}\text{Tb}_{14}$  [12]. The fit yields a magnetic moment magnitude of  $7.86(13)\mu_B$ .

#### IV. DISCUSSION

The direction of the magnetic moment should reflect the easy-axis anisotropy of the Tb atom induced by the crystalline electric field. The easy-axis nature of the magnetic moment

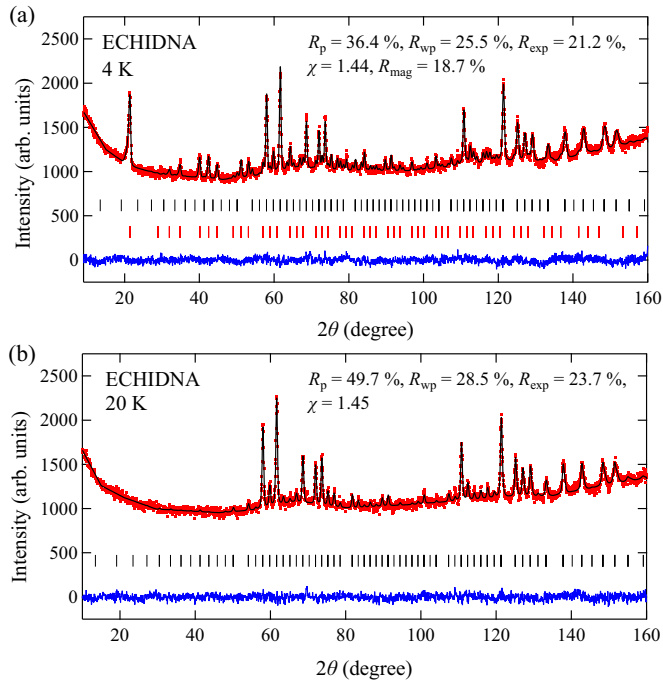


FIG. 3. Powder neutron diffraction patterns measured at (a) 4 K and (b) 20 K. The observed intensities, calculated intensities, and their differences are represented by red dots and black and blue curves, respectively. The positions of the nuclear and magnetic reflections are indicated by black and red solid lines, respectively.

on the Tb atom is indicated in  $\text{Tb}_6\text{Cd}$  and  $\text{Au}_{70}\text{Si}_{17}\text{Tb}_{13}$ . An analysis of the inelastic neutron spectrum assuming local pentagonal symmetry [32] suggests that the easy-axis direction is along the pseudofivefold symmetry axis in  $\text{Cd}_6\text{Tb}$  [33]. However, neutron diffraction and inelastic neutron scattering studies indicate that the easy-axis direction is perpendicular to the pseudofivefold symmetry axis in  $\text{Au}_{70}\text{Si}_{17}\text{Tb}_{13}$  [13]. As shown in Fig. 1(b), the direction of the magnetic moment observed in  $\text{Au}_{65}\text{Ga}_{21}\text{Tb}_{14}$  (which is almost equivalent to that in  $\text{Au}_{72}\text{Al}_{14}\text{Tb}_{14}$ ) is perpendicular to the pseudofivefold symmetry axis. Thus, the easy-axis direction should also be perpendicular to the pseudofivefold symmetry axis in these compounds. According to the crystalline electric field calculations based on the point charge model, the easy-axis direction can range between the directions parallel and perpendicular to the pseudofivefold symmetry axis, depending on the ratio of the effective valences of the ligand atoms [16]. The similarity in the directions of the magnetic moments between  $\text{Au}_{72}\text{Al}_{14}\text{Tb}_{14}$  and  $\text{Au}_{65}\text{Ga}_{21}\text{Tb}_{14}$  indicates that the ground-state wave function of  $\text{Tb}^{3+}$  ions is almost unchanged, despite the large difference in the occupancy of the Ga2 (Au2) atom. The change in the crystalline electric field may be suppressed by the screening effect of conduction electrons.

The macroscopic magnetic properties suggest that ferromagnetic interactions are enhanced in  $\text{Au}_{65}\text{Ga}_{21}\text{Tb}_{14}$  compared with those of  $\text{Au}_{72}\text{Al}_{14}\text{Tb}_{14}$ . The possible nearest-neighbor ( $J_1$ ) and next-nearest-neighbor ( $J_2$ ) interactions were estimated by reproducing the magnetization curve. The simulation was performed based on a single cluster composed of Ising spins following the procedure presented in Ref. [12].

The cluster is regarded as an icosahedron with two types of Heisenberg interactions:

$$H = -J_1 \sum_{\text{NN}} \sigma_i \cdot \sigma_j - J_2 \sum_{\text{NNN}} \sigma_i \cdot \sigma_j + g\mu_B H \sum_i \sigma_i, \quad (1)$$

where  $\sigma_i$  ( $i = 1, 2$ ) is an Ising spin with the total angular momentum of the Tb atoms ( $\sigma_{iz} = \pm J$ , with  $J = 6$ ).  $J_1$  and  $J_2$  represent the magnetic interactions coupled to the five nearest- and five next-nearest-neighbor sites, respectively. In this model, the metamagnetic transition is regarded as the spin reorientation of the magnetic moments in an icosahedron. With an increase in the magnetic field, half of the magnetic moments were flipped in the opposite direction, as shown in Fig. 1(d). This results in a large increase in magnetization at a finite field. In addition, the differences in symmetry over the metamagnetic transition naturally explain its first-order nature. The ferromagnetic interactions of  $J_1 = 0.0221$  K and  $J_2 = 0.132$  K reproduced the experimental data well, as shown by the black solid curve in Fig. 2(d). They also yielded a Weiss temperature of  $\theta_W = 5J(J+1)(J_1+J_2)/3 = 10.8$  K ( $J = 6$ ), consistent with that estimated experimentally. Furthermore, these interactions are compatible with the occurrence of antiferromagnetic order, which is stable under the condition  $J_1 < J_2/2$  [12,18].

Let us compare the magnetic properties of  $\text{Au}_{65}\text{Ga}_{21}\text{Tb}_{14}$  and  $\text{Au}_{72}\text{Al}_{14}\text{Tb}_{14}$ , both of which are confirmed to have the magnetic structure illustrated in Fig. 1(c). The  $e/a$  values of the two compounds are 1.70 and 1.56, respectively. A large  $e/a$  is qualitatively consistent with enhanced ferromagnetic interactions, according to the phase diagram established from the magnetization measurements of a series of magnetic quasicrystal approximants [8,9,18]. A further increase in the  $e/a$  value enhances ferromagnetic interactions and results in a ferromagnetic order similar to that observed in  $\text{Au}_{70}\text{Si}_{17}\text{Tb}_{13}$  [13]. The magnetic structure of  $\text{Au}_{70}\text{Si}_{17}\text{Tb}_{13}$  is almost the same as that of  $\text{Au}_{65}\text{Ga}_{21}\text{Tb}_{14}$  under a magnetic field, which is illustrated in Fig. 1(d). The magnetic structures of  $\text{Au}_{72}\text{Al}_{14}\text{Tb}_{14}$  ( $e/a = 1.56$ ),  $\text{Au}_{65}\text{Ga}_{21}\text{Tb}_{14}$  ( $e/a = 1.72$ ), and  $\text{Au}_{70}\text{Si}_{17}\text{Tb}_{13}$  ( $e/a = 1.77$ ) strongly support the idea that the magnetic moment of a Tb atom behaves as an Ising spin in the Tb-based quasicrystal approximant. The direction of the principal axes of the Tb atom does not change significantly with the change in composition, whereas the direction of the magnetic moments [selection of the magnetic structure shown in Figs. 1(c) or 1(d)] is determined by the magnetic interactions between Tb atoms. However, it remains unclear how magnetic interactions and magnetic structures are modified by tuning the  $e/a$  value. It would be interesting to investigate the effective magnetic exchanges using inelastic neutron scattering experiments to understand this mechanism.

## V. CONCLUSION

A whirling antiferromagnetic magnetic order was observed in the quasicrystal approximant  $\text{Au}_{65}\text{Ga}_{21}\text{Tb}_{14}$ . Magnetization measurements and neutron diffraction experiments indicate that the antiferromagnetic order is induced by the ferromagnetic next-nearest-neighbor interactions and the easy-axis anisotropy of the Tb atom. Despite the large difference in the occupancy ratio of the chemically disordered atoms at

some ligand sites, the direction of the magnetic moment in the antiferromagnetic phase is almost the same as that in  $\text{Au}_{72}\text{Al}_{14}\text{Tb}_{14}$ . The negligible influence of chemical substitution on the easy-axis direction suggests that the crystalline electric field can be screened by the conduction electrons in magnetic quasicrystal approximants.

### ACKNOWLEDGMENTS

This study was supported by Grants-in-Aid for Early Career Scientists (Grant No. 20K14395), Scientific Research on Innovative Areas (Grants No. 19H05818, No. 19H05819, No. 20H05261, and No. 22H04582), Scientific Research (B) (Grant No. 19H01834), the Fund for the Promotion of Joint International Research (Fostering Joint International Research; Grant No. 18KK0150) from the Japan Society for the Promotion of Science, and the CORE Laboratory Research Program ‘‘Dynamic Alliance for Open Innovation Bridging Human, Environment and Materials’’ of the Network Joint Research Center for Materials and Device and a Grant for Basic Science Research Projects of the Sumitomo Foundation. The experiments at JRR-3 and the travel expenses for the neutron scattering experiment at ANSTO were partly supported by the General User Program for Neutron Scattering Experiments, Institute for Solid State Physics, University of Tokyo. K.N. thanks S. Kameoka for his help in performing the powder XRD experiments.

### APPENDIX A: PARALLEL AND PERPENDICULAR SUSCEPTIBILITY UNDER ANISOTROPY

In this Appendix, we discuss the magnetic susceptibility of quasicrystal approximants consisting of rare-earth atoms with strong easy-axis (or easy-plane) anisotropy. Previous inelastic neutron scattering studies on the quasicrystal approximant  $\text{Au}_{70}\text{Si}_{17}\text{Tb}_{13}$  indicated that the second-order uniaxial term dominates the anisotropy of  $\text{Tb}^{3+}$  ions [13]. Thus, the crystal electric field Hamiltonian can be simplified as

$$H_0 = -D\hat{J}_z^2. \quad (\text{A1})$$

In the following discussion, we assume that the angular momentum quantum number  $J$  is an integer and  $D$  is positive. A schematic view of energy levels and eigenfunctions under this assumption is illustrated in Fig. 4. The ground states consist of a degenerate non-Kramers doublet,  $|J, J_z = \pm J\rangle$ . Energy levels of  $|J, J_z = \pm j\rangle$  states become higher as  $j$  becomes smaller.

A magnetic field induces hybridization between these eigenstates, leading to a shift of each energy level. The energy of the  $|J, J_z = j\rangle$  state can be calculated by regarding the magnetic field as a perturbation,

$$E_j^\alpha = E_{j0} - g\mu_B H I_{jj}^\alpha - (g\mu_B H)^2 \sum_{j' \neq j} \frac{|I_{jj'}^\alpha|^2}{E_{j'} - E_j}, \quad (\text{A2})$$

where  $E_{j0} = -Dj^2$  and  $I_{\alpha}^{jj'} = \langle J, j | \hat{J}_\alpha | J, j' \rangle$ . The magnetic susceptibility along the  $\alpha$  direction becomes

$$\chi_\alpha = Ng^2\mu_B^2 \left\{ \sum_j \beta I_{\alpha}^{jj^2} \frac{e^{-\beta E_{j0}}}{Z} - \left( \sum_j I_{\alpha}^{jj} \frac{e^{-\beta E_{j0}}}{Z} \right)^2 + 2 \sum_j \sum_{j' \neq j} \frac{|I_{\alpha}^{jj'}|^2}{E_{j'0} - E_{j0}} \frac{e^{-\beta E_{j0}}}{Z} \right\}, \quad (\text{A3})$$

where  $Z$  represents the partition function. For instance, the energies under a magnetic field along and perpendicular to the anisotropy axis ( $z$ ) are

$$E_{\parallel}(j) = -Dj^2 - g\mu_B H j, \quad (\text{A4})$$

$$E_{\perp}(j) = -Dj^2 - \frac{(g\mu_B H)^2}{D} \left\{ \frac{J(J+1) - j(j-1)}{j^2 - (j-1)^2} + \frac{J(J+1) - j(j+1)}{(j+1)^2 - j^2} \right\}, \quad (\text{A5})$$

respectively. From the partition function

$$Z_{\parallel} = \sum_{j=-J}^J e^{-\beta E_{\parallel}(j)}, \quad (\text{A6})$$

$$Z_{\perp} = \sum_{j=-J}^J e^{-\beta E_{\perp}(j)}, \quad (\text{A7})$$

the magnetic susceptibility becomes

$$\chi_{\parallel} = Ng^2\mu_B^2 \beta \frac{2 \sum_{j=1}^J j^2 e^{j^2 D \beta}}{1 + 2 \sum_{j=1}^J e^{j^2 D \beta}}, \quad (\text{A8})$$

$$\chi_{\perp} = \frac{Ng^2\mu_B^2}{D} \frac{\sum_{j=1}^J \frac{J(J+1) - j(j-1)}{j^2 - (j-1)^2} (e^{j^2 D \beta} - e^{(j-1)^2 D \beta})}{1 + 2 \sum_{j=1}^J e^{j^2 D \beta}}. \quad (\text{A9})$$

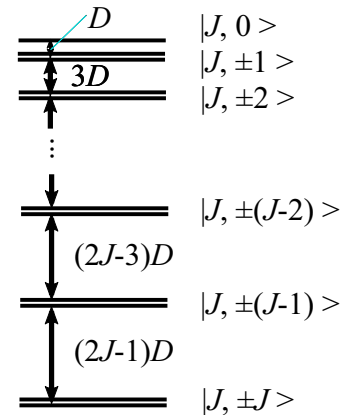


FIG. 4. Schematic view of energy levels and eigenfunctions  $|J, J_z\rangle$  of a rare-earth atom under the model Hamiltonian (A1) with easy-axis anisotropy ( $D > 0$ ).

It is convenient to derive their series expansions around  $\beta \sim 0$  to discuss the temperature dependence at high temperatures as

$$\begin{aligned} \chi_{\parallel} &= Ng^2\mu_B^2\beta\frac{1}{3}J(J+1) \\ &\times \left\{ 1 + \frac{1}{15}(2J-1)(2J+3)(D\beta) \right. \\ &+ \frac{1}{630}(2J-3)(2J-1)(2J+3)(2J+5)(D\beta)^2 \\ &\left. + \dots \right\}, \end{aligned} \quad (\text{A10})$$

$$\begin{aligned} \chi_{\perp} &= Ng^2\mu_B^2\beta\frac{1}{3}J(J+1) \\ &\times \left\{ 1 - \frac{1}{30}(2J-1)(2J+3)(D\beta) \right. \\ &- \frac{1}{630}(2J-1)(2J+3)(2J^2+2J+3)(D\beta)^2 \\ &\left. + \dots \right\}. \end{aligned} \quad (\text{A11})$$

As discussed in Appendix B, the bulk magnetic susceptibility is given by an average of the local magnetic susceptibility among several rare-earth atoms that have different orientations of principal axes. It becomes a powder-averaged form as

$$\begin{aligned} \bar{\chi} &= \frac{1}{3}(\chi_{\parallel} + 2\chi_{\perp}) \\ &= Ng^2\mu_B^2\beta\frac{1}{3}J(J+1) \\ &\times \left\{ 1 - \frac{1}{90}(2J-1)(2J+3)(D\beta)^2 + \dots \right\}. \end{aligned} \quad (\text{A12})$$

The first-order term with respect to  $\beta$  represents the Curie law of free rare-earth atoms. On the other hand, the second-order term, whose coefficient corresponds to the Weiss temperature, is absent in Eq. (A12). Usually, uniaxial anisotropy contributes to the second-order term such as that presented in Eqs. (A10) and (A11). However, its contribution is canceled by taking an average of the local magnetic susceptibility among several rare-earth atoms with different principal axes. Consequently, the magnetic susceptibility at high temperatures follows the Curie rule well. Note that magnetic interactions between rare-earth atoms are absent in the above discussion. The magnetic interactions between rare-earth atoms would act as the molecular field, leading to the temperature dependence following the Curie-Weiss rule.

The temperature range where the Curie-Weiss fit could be applicable depends on the magnitude of  $J$  and  $D$ . Finally, let us discuss the temperature range valid for the Curie-Weiss fit in the Tb-based quasicrystal approximant.  $J$  becomes 6 for  $\text{Tb}^{3+}$ . The estimated averaged coefficient of the dominant second-order uniaxial term  $\bar{q}_{20} = -0.007$  of  $\text{Au}_{70}\text{Si}_{17}\text{Tb}_{13}$  [13] corresponds to a  $D$  value of 4 K. From these values, the third-order term of  $\beta$  is estimated to be almost 1% of the Curie term from Eq. (A12). Figure 5 shows temperature dependences of the inverse magnetic susceptibility derived by substituting  $J = 6$  and  $D = 4$  K in Eqs. (A8) and (A9). Compared with the parallel and perpendicular inverse susceptibilities, the averaged inverse susceptibility is quite close to a straight line. In addition, the intercept of the line is almost zero. This is also clear from the small deviation from the Curie rule, as shown in the inset of Fig. 5. The deviation from the ideal value is kept to almost within 1% above 50 K, which is consistent with the estimate from the series expansion. The small deviation ensures the validity of the Curie-Weiss fit, which is performed above 50 K in this study.

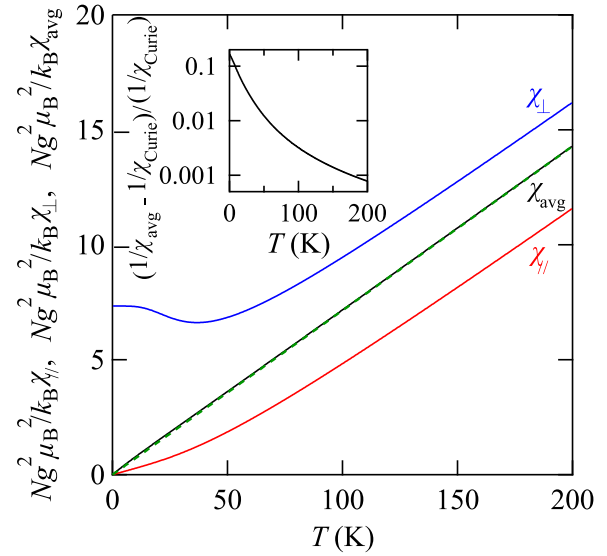


FIG. 5. Temperature dependences of inverse magnetic susceptibility. The inverse of parallel (red), perpendicular (blue), and averaged (black) susceptibility multiplied by a normalization factor is plotted as a function of temperature. The green dashed line indicates the Curie rule expected for free  $\text{Tb}^{3+}$  ions. The inset shows the deviation of the inverse susceptibility against the Curie rule.

The above discussion can also be applied to rare-earth atoms that have Kramers doublets as eigenstates. Applying a perturbation theory to degenerate Kramers doublets,  $|J, J_z = \pm(J-1/2)\rangle, \dots, |J, J_z = \pm 1/2\rangle$ , leads to the parallel and perpendicular magnetic susceptibilities

$$\begin{aligned} \chi_{\parallel} &= Ng^2\mu_B^2\beta \frac{\sum_{j=1}^J (j - \frac{1}{2})^2 e^{(j-\frac{1}{2})^2 D\beta}}{\sum_{j=1}^J e^{(j-\frac{1}{2})^2 D\beta}}, \quad (\text{A13}) \\ \chi_{\perp} &= Ng^2\mu_B^2 \left\{ \frac{1}{2D \sum_{j=1}^J e^{(j-\frac{1}{2})^2 D\beta}} \right. \\ &\times \sum_{j=1}^{J-1} \frac{(J - \frac{1}{2})(J + \frac{1}{2}) - (j + 1/2)(j - 1/2)}{(j + 1/2)^2 - (j - 1/2)^2} \\ &\times (e^{(j+1/2)^2 D\beta} - e^{(j-1/2)^2 D\beta}) \\ &\left. + \beta \frac{J^2 e^{\frac{D\beta}{4}}}{4 \sum_{j=1}^J e^{(j-\frac{1}{2})^2 D\beta}} \right\}. \end{aligned} \quad (\text{A14})$$

The second-order term of  $\beta$  is confirmed to be zero from series expansion of the averaged susceptibility.

## APPENDIX B: CONTRIBUTION OF THE LOCAL PARALLEL AND PERPENDICULAR SUSCEPTIBILITIES TO THE BULK SUSCEPTIBILITY

In this section, the contribution of the local parallel and perpendicular magnetic susceptibilities to the bulk magnetic susceptibility is discussed. In the 1/1 quasicrystal approximant, a single cluster is composed of 12 rare-earth atoms, which have the atomic coordination listed in Table III. The bulk magnetic susceptibility corresponds to an average of the local magnetic susceptibility among the 12 rare-earth

TABLE III. List of the coordinates of Tb atoms in a unit cell. The rest of the half atoms are induced by centering symmetry  $+(1/2, 1/2, 1/2)$ .

Tb atoms	Atomic coordinates		
Tb1	0	$y_0$	$z_0$
Tb2	0	$-y_0+1$	$z_0$
Tb3	0	$y_0$	$-z_0+1$
Tb4	0	$-y_0+1$	$-z_0+1$
Tb5	$z_0$	0	$y_0$
Tb6	$z_0$	0	$-y_0+1$
Tb7	$-z_0+1$	0	$y_0$
Tb8	$-z_0+1$	0	$-y_0+1$
Tb9	$y_0$	$z_0$	0
Tb10	$-y_0+1$	$z_0$	0
Tb11	$y_0$	$-z_0+1$	0
Tb12	$-y_0+1$	$-z_0+1$	0

atoms, which have different orientations of the principal axes. To obtain the averaged magnetic susceptibility, let us derive the relation between global and local angular momentum operators and then rewrite the bulk magnetic susceptibility in terms of the local angular momentum operators. In the following, we introduce the global angular momentum operators  $\hat{J}_x$ ,  $\hat{J}_y$ , and  $\hat{J}_z$  along a magnetic field direction  $\mathbf{h} = (\sin \theta \cos \psi, \sin \theta \sin \psi, \cos \theta)$ . Following Eq. (A3), the magnetic susceptibility along this direction at the  $i$ th rare-earth atom is given by

$$\chi_{ih} = N g^2 \mu_B^2 \left\{ \sum_j \beta I_{ih}^{jj^2} \frac{e^{-\beta E_{j0}}}{Z} - \left( \sum_j I_{ih}^{jj} \frac{e^{-\beta E_{j0}}}{Z} \right)^2 + 2 \sum_j \sum_{j' \neq j} \frac{|I_{ih}^{jj'}|^2}{E_{j'0} - E_{j0}} \frac{e^{-\beta E_{j0}}}{Z} \right\}, \quad (\text{B1})$$

where

$$I_{ih}^{jj'} = \langle \Psi_j | \hat{J}_h | \Psi_{j'} \rangle_i, \quad \hat{J}_h = \hat{J}_x \sin \theta \cos \psi + \hat{J}_y \sin \theta \sin \psi + \hat{J}_z \cos \theta. \quad (\text{B2})$$

Equation (B1) is applicable to any system as long as non-diagonal matrix elements of degenerate eigenstates are zero

( $I_{ih}^{jj'} = 0$ , where  $j \neq j'$  and  $E_j = E_{j'}$ ). Note that the wave function  $|\Psi_j\rangle_i$  is defined at the  $i$ th atom, which is represented by the subscript of a ket vector.  $I_{ih}^{jj'}$  depends on  $i$  since the magnetic field direction becomes effectively different in each rare-earth atom. The averaged magnetic susceptibility among 12 rare-earth atoms becomes

$$\bar{\chi}_h \equiv \frac{1}{12} \sum_{i=1}^{12} \chi_{ih} = \frac{N g^2 \mu_B^2}{12} \left\{ \sum_j \beta \left( \sum_{i=1}^{12} I_{ih}^{jj^2} \right) \frac{e^{-\beta E_{j0}}}{Z} - \sum_j \sum_{j'} \left( \sum_{i=1}^{12} I_{ih}^{jj'} I_{ih}^{j'j} \right) \frac{e^{-\beta(E_{j0}+E_{j'0})}}{Z^2} + 2 \sum_j \sum_{j' \neq j} \left( \sum_{i=1}^{12} |I_{ih}^{jj'}|^2 \right) \frac{1}{E_{j'0} - E_{j0}} \frac{e^{-\beta E_{j0}}}{Z} \right\}. \quad (\text{B3})$$

First, we derive the magnetic susceptibility of the rare-earth atom with the atomic coordination  $(0, y_0, z_0)$  (the Tb1 site in Table III). Because of a mirror symmetry with respect to the  $bc$  plane, one of the local principal axes should be along the  $a$  direction. Thus, the local principal axes,  $1x$ ,  $1y$ , and  $1z$ , can be defined as

$$(\mathbf{e}_{1x} \ \mathbf{e}_{1y} \ \mathbf{e}_{1z}) = (\mathbf{e}_x \ \mathbf{e}_y \ \mathbf{e}_z) \begin{pmatrix} 1 & 0 & 0 \\ 0 & \cos \theta_a & -\sin \theta_a \\ 0 & \sin \theta_a & \cos \theta_a \end{pmatrix}, \quad (\text{B4})$$

where  $\mathbf{e}_x$ ,  $\mathbf{e}_y$ , and  $\mathbf{e}_z$  represent the global  $a$ ,  $b$ , and  $c$  axes of the cubic lattice, respectively. The definition of the local principal axes is schematically illustrated in Fig. 6. The wave function defined in the global frame is modified to that defined in the local frame by the rotation around the  $x$  axis as  $|\Psi_j\rangle_i \rightarrow e^{-i\theta_a \hat{J}_x} |\Psi_j\rangle_i$ . Local magnetization along the magnetic field direction is given by

$$I_{1h}^{jj'} \equiv \langle \Psi_j | e^{i\theta_a \hat{J}_x} \hat{J}_h e^{-i\theta_a \hat{J}_x} | \Psi_{j'} \rangle_1. \quad (\text{B5})$$

$I_{1h}^{jj'}$  can be rewritten in terms of the magnetization along the principal axes  $I_{\alpha}^{jj'} \equiv \langle \Psi_j | \hat{J}_{i\alpha} | \Psi_{j'} \rangle_i$  ( $\alpha = x, y, z$ ) from Eqs. (B2) and (B5) as

$$J_{1h} \equiv e^{i\theta_a \hat{J}_x} \hat{J}_h e^{-i\theta_a \hat{J}_x} = \hat{J}_{1x} \sin \theta \cos \psi + (\hat{J}_{1y} \sin \theta \sin \psi + \hat{J}_{1z} \cos \theta) \cos \theta_a + (\hat{J}_{1y} \cos \theta - \hat{J}_{1z} \sin \theta \sin \psi) \sin \theta_a$$

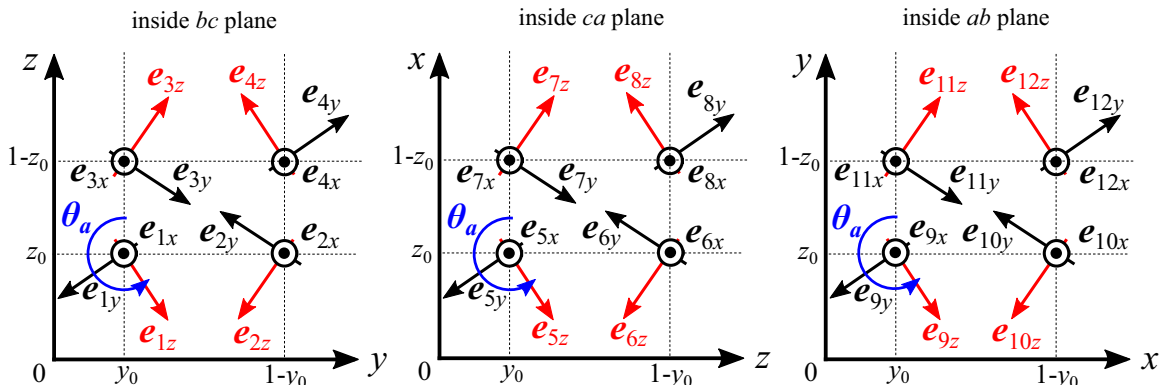


FIG. 6. Direction of local principal axes of Tb1–Tb12 atoms. The directions of the  $z$  axes are highlighted in red.



$$I_{11h}^{jj'} = \langle \Psi_j | J_{1h} | \Psi_{j'} \rangle_1$$

$$= \{ I_x^{jj'} \sin \theta \cos \psi + (I_y^{jj'} \sin \theta \sin \psi + I_z^{jj'} \cos \theta) \cos \theta_a$$

$$+ (I_y^{jj'} \cos \theta - I_z^{jj'} \sin \theta \sin \psi) \sin \theta_a \}. \quad (\text{B6})$$

Note that  $I_a^{jj'}$  does not depend on  $i$  as all the rare-earth atoms are symmetrically equivalent.

The same procedure can be applied to the all 12 rare-earth atoms. The matrix element for the second rare-earth atom (the Tb2 site in Table III) becomes

$$I_{2h}^{jj'} \equiv \langle \Psi_j | e^{-i\theta_a \hat{J}_x} \hat{J}_h e^{i\theta_a \hat{J}_x} | \Psi_{j'} \rangle_2, \quad (\text{B7})$$

and from Eqs. (B2) and (B7),

$$J_{2h} \equiv e^{-i\theta_a \hat{J}_x} \hat{J}_h e^{i\theta_a \hat{J}_x} = \hat{J}_x \sin \theta \cos \psi$$

$$+ (\hat{J}_y \sin \theta \sin \psi + \hat{J}_z \cos \theta) \cos \theta_a$$

$$- (\hat{J}_y \cos \theta - \hat{J}_z \sin \theta \sin \psi) \sin \theta_a,$$

$$I_{22h}^{jj'} = \{ I_x^{jj'} \sin \theta \cos \psi$$

$$+ (I_y^{jj'} \sin \theta \sin \psi + I_z^{jj'} \cos \theta) \cos \theta_a$$

$$- (I_y^{jj'} \cos \theta - I_z^{jj'} \sin \theta \sin \psi) \sin \theta_a \}. \quad (\text{B8})$$

The same procedure for the Tb3 and Tb4 atoms results in

$$I_{33h}^{jj'} = \{ I_x^{jj'} \sin \theta \cos \psi$$

$$- (I_y^{jj'} \sin \theta \sin \psi + I_z^{jj'} \cos \theta) \cos \theta_a$$

$$+ (I_y^{jj'} \cos \theta - I_z^{jj'} \sin \theta \sin \psi) \sin \theta_a \},$$

$$I_{44h}^{jj'} = \{ I_x^{jj'} \sin \theta \cos \psi$$

$$- (I_y^{jj'} \sin \theta \sin \psi + I_z^{jj'} \cos \theta) \cos \theta_a$$

$$- (I_y^{jj'} \cos \theta - I_z^{jj'} \sin \theta \sin \psi) \sin \theta_a \}, \quad (\text{B9})$$

respectively. Thus, the sum of  $I_{ih}^{jj'2}$  over the Tb1–Tb4 atoms becomes

$$\sum_{i=1}^4 I_{ih}^{jj'2} = 4 \{ I_x^{jj'2} \sin^2 \theta \cos^2 \psi$$

$$+ I_y^{jj'2} (\sin^2 \theta \sin^2 \psi \cos^2 \theta_a + \cos^2 \theta \sin^2 \theta_a)$$

$$+ I_z^{jj'2} (\sin^2 \theta \sin^2 \psi \sin^2 \theta_a + \cos^2 \theta \cos^2 \theta_a)$$

$$+ 2 I_x^{jj'} I_y^{jj'} \sin \theta \cos \theta \sin \psi (\cos^2 \theta_a - \sin^2 \theta_a) \}. \quad (\text{B10})$$

The corresponding sums over the Tb5–Tb8 and Tb9–Tb12 atoms are given in a similar form as

$$\sum_{i=5}^8 I_{ih}^{jj'2} = 4 \{ I_y^{jj'2} \sin^2 \theta \cos^2 \psi$$

$$+ I_z^{jj'2} (\sin^2 \theta \sin^2 \psi \cos^2 \theta_a + \cos^2 \theta \sin^2 \theta_a)$$

$$+ I_x^{jj'2} (\sin^2 \theta \sin^2 \psi \sin^2 \theta_a + \cos^2 \theta \cos^2 \theta_a)$$

$$+ 2 I_z^{jj'} I_x^{jj'} \sin \theta \cos \theta \sin \psi (\cos^2 \theta_a - \sin^2 \theta_a) \}. \quad (\text{B11})$$

and

$$\sum_{i=9}^{12} I_{ih}^{jj'2} = 4 \{ I_z^{jj'2} \sin^2 \theta \cos^2 \psi$$

$$+ I_x^{jj'2} (\sin^2 \theta \sin^2 \psi \cos^2 \theta_a + \cos^2 \theta \sin^2 \theta_a)$$

$$+ I_y^{jj'2} (\sin^2 \theta \sin^2 \psi \sin^2 \theta_a + \cos^2 \theta \cos^2 \theta_a)$$

$$+ 2 I_x^{jj'} I_y^{jj'} \sin \theta \cos \theta \sin \psi (\cos^2 \theta_a - \sin^2 \theta_a) \}, \quad (\text{B12})$$

respectively. The sum of Eqs. (B10), (B11), and (B12) is

$$\frac{1}{12} \sum_{i=1}^{12} I_{ih}^{jj'2} = \frac{1}{3} \{ I_x^{jj'2} + I_y^{jj'2} + I_z^{jj'2}$$

$$+ 2 (I_x^{jj'} I_y^{jj'} + I_y^{jj'} I_z^{jj'} + I_z^{jj'} I_x^{jj'})$$

$$\times \sin \theta \cos \theta \sin \psi (\cos^2 \theta_a - \sin^2 \theta_a) \}. \quad (\text{B13})$$

Due to the threefold symmetry in the quasicrystal approximant, the magnetic field direction dependence of the magnetic susceptibility can be symmetrized as

$$\frac{1}{12} \sum_{i=1}^{12} I_{ih}^{jj'2} = \frac{1}{3} \{ I_x^{jj'2} + I_y^{jj'2} + I_z^{jj'2}$$

$$+ \frac{2}{3} (I_x^{jj'} I_y^{jj'} + I_y^{jj'} I_z^{jj'} + I_z^{jj'} I_x^{jj'})$$

$$\times (\sin^2 \theta \cos \psi \sin \psi + \sin \theta \cos \theta \sin \psi$$

$$+ \sin \theta \cos \theta \cos \psi) (\cos^2 \theta_a - \sin^2 \theta_a) \}. \quad (\text{B14})$$

The sum of  $I_{ih}^{jj'} I_{ih}^{j'j}$  and  $|I_{ih}^{jj'}|^2$  can be also obtained in the same manner.

The magnetic field direction dependence in Eq. (B14) disappears in some simple cases. For instance, if the Hamiltonian is given by Eq. (A1) and the angular momentum quantum number  $J$  is an integer,  $|\Psi_j\rangle$  can be replaced by  $|J, j\rangle$  ( $j = 0, \dots, J$ ). Then, only  $I_z^{jj}$ ,  $I_x^{jj\pm 1}$ , and  $I_y^{jj\pm 1}$  become nonzero for diagonal components. In addition, some matrix elements from nondiagonal components are canceled ( $I_x^{jj'} I_y^{j'j*} + I_x^{j'j*} I_y^{jj'} = 0$ ). Consequently, the averaged magnetic susceptibility is simplified as

$$\overline{\chi}_h = \frac{1}{3} (\chi_x + \chi_y + \chi_z), \quad (\text{B15})$$

where  $\chi_\alpha$  represents the local magnetic susceptibility along the principal axes ( $\alpha = x, y, z$ ). Equation (B15) indicates that the bulk magnetic susceptibility is equal to the powder-averaged form of the local magnetic susceptibility irrespective of the local magnetic anisotropy and the magnetic field direction if the crystal field Hamiltonian consists of only the second-order term of  $\hat{J}_z$ . The magnetic anisotropy recovers through the coexistence of additional terms. The same consequence can be derived for rare-earth ions with a half-integer  $J$ .

- [1] A. P. Tsai, J. Q. Guo, E. Abe, H. Takakura, and T. J. Sato, *Nature (London)* **408**, 537 (2000).
- [2] A. I. Goldman, T. Kong, A. Kreyssig, A. Jesche, M. Ramazanoglu, K. W. Dennis, S. L. Budko, and P. C. Canfield, *Nat. Mater.* **12**, 714 (2013).
- [3] R. Tamura, Y. Muro, T. Hiroto, K. Nishimoto, and T. Takabatake, *Phys. Rev. B* **82**, 220201(R) (2010).
- [4] M. G. Kim, G. Beutier, A. Kreyssig, T. Hiroto, T. Yamada, J. W. Kim, M. de Boissieu, R. Tamura, and A. I. Goldman, *Phys. Rev. B* **85**, 134442 (2012).
- [5] D. H. Ryan, J. M. Cadogan, T. Kong, P. C. Canfield, A. I. Goldman, and A. Kreyssig, *AIP Adv.* **9**, 035312 (2019).
- [6] R. Tamura, Y. Murao, S. Takeuchi, M. Ichihara, M. Isobe, and Y. Ueda, *Jpn. J. Appl. Phys.* **41**, L524 (2002).
- [7] K. Nishimoto, T. Sato, and R. Tamura, *J. Phys.: Condens. Matter* **25**, 235403 (2013).
- [8] A. Ishikawa, T. Hiroto, K. Tokiwa, T. Fujii, and R. Tamura, *Phys. Rev. B* **93**, 024416 (2016).
- [9] A. Ishikawa, T. Fujii, T. Takeuchi, T. Yamada, Y. Matsushita, and R. Tamura, *Phys. Rev. B* **98**, 220403(R) (2018).
- [10] T. Hiroto, G. H. Gebresenbut, C. P. Gómez, Y. Muro, M. Isobe, Y. Ueda, K. Tokiwa, and R. Tamura, *J. Phys.: Condens. Matter* **25**, 426004 (2013).
- [11] G. Gebresenbut, M. S. Andersson, P. Beran, P. Manuel, P. Nordblad, M. Sahlberg, and C. P. Gomez, *J. Phys.: Condens. Matter* **26**, 322202 (2014).
- [12] T. J. Sato, A. Ishikawa, A. Sakurai, M. Hattori, M. Avdeev, and R. Tamura, *Phys. Rev. B* **100**, 054417 (2019).
- [13] T. Hiroto, T. J. Sato, H. Cao, T. Hawaii, T. Yokoo, S. Itoh, and R. Tamura, *J. Phys.: Condens. Matter* **32**, 415802 (2020).
- [14] G. H. Gebresenbut, T. Shiino, M. S. Andersson, N. Qureshi, O. Fabelo, P. Beran, D. Qvarngård, P. Henelius, A. Rydh, R. Mathieu, P. Nordblad, and C. Pay Gomez, *Phys. Rev. B* **106**, 184413 (2022).
- [15] K. Nawa, D. Okuyama, A. Ebina, T. J. Sato, A. Ishikawa, and R. Tamura, *J. Phys.: Conf. Ser.* **2461**, 012015 (2023).
- [16] S. Watanabe, *Proc. Natl. Acad. Sci. USA* **118**, e2112202118 (2021).
- [17] S. Suzuki, R. Tamura, and T. Sugimoto, *Mater. Trans.* **62**, 367 (2021).
- [18] S. Suzuki, A. Ishikawa, T. Yamada, T. Sugimoto, A. Sakurai, and R. Tamura, *Mater. Trans.* **62**, 298 (2021).
- [19] S. Watanabe and M. Kawamoto, *J. Phys. Soc. Jpn.* **90**, 063701 (2021).
- [20] K. Inagaki, A. Ishikawa, T. Hiroto, K. Tokiwa, T. Fujii, and R. Tamura, Abstracts from the 9th Conference on Aperiodic Crystals, Vol. 1 (2018) (unpublished).
- [21] R. Tamura, A. Ishikawa, S. Suzuki, T. Kotajima, Y. Tanaka, T. Seki, N. Shibata, T. Yamada, T. Fujii, C.-W. Wang, M. Avdeev, K. Nawa, D. Okuyama, and T. J. Sato, *J. Am. Chem. Soc.* **143**, 19938 (2021).
- [22] Rigaku Oxford Diffraction, CRYCALISPRO, Yarnton, UK, 2018.
- [23] G. M. Sheldrick, *Acta Crystallogr., Sect. A* **71**, 3 (2015).
- [24] G. M. Sheldrick, *Acta Crystallogr., Sect. C* **71**, 3 (2015).
- [25] M. Avdeev and J. R. Hester, *J. Appl. Crystallogr.* **51**, 1597 (2018).
- [26] K. Momma and F. Izumi, *J. Appl. Crystallogr.* **44**, 1272 (2011).
- [27] See Supplemental Material at <http://link.aps.org/supplemental/10.1103/PhysRevMaterials.7.054412> for structural parameters and crystallographic data for powder x-ray and neutron diffraction experiments.
- [28] R. Guida and J. Zinn-Justin, *J. Phys. A* **31**, 8103 (1998).
- [29] T. Shiino, G. H. Gebresenbut, C. P. Gómez, U. Häussermann, P. Nordblad, A. Rydh, and R. Mathieu, *Phys. Rev. B* **106**, 174405 (2022).
- [30] Y. Izyumov and V. Naish, *J. Magn. Magn. Mater.* **12**, 239 (1979).
- [31] J. Rodríguez-Carvajal, BASIREPS, <https://www.ill.eu/sites/fullprof/php/programsfa7c.html?pagina=GBasireps>.
- [32] S. Jazbec, S. Kashimoto, P. Koželj, S. Vrtnik, M. Jagodič, Z. Jagličić, and J. Dolinšek, *Phys. Rev. B* **93**, 054208 (2016).
- [33] P. Das, P.-F. Lory, R. Flint, T. Kong, T. Hiroto, S. L. Bud'ko, P. C. Canfield, M. de Boissieu, A. Kreyssig, and A. I. Goldman, *Phys. Rev. B* **95**, 054408 (2017).